algorithms

MDPI

Article

Multiscale Model—Differential Evolutionary Algorithm for Inverse Solution of T-Wave Inversion in Electrocardiography

Tengda Guo, Junjiang Zhu * and Yunjie Li

College of Electrical and Mechanical Engineering, China Jiliang University, Hangzhou 310018, China
* Correspondence: zhujunjiang@cjlu.edu.cn

Abstract

T-wave inversion (TWI) on an electrocardiogram (ECG) is a key indicator of myocardial ischemia, yet existing inverse ECG methods lack quantitative physiological parameter resolution. This study aims to propose a novel multiscale computational framework to inversely identify the ionic mechanisms underlying TWI. A cell–tissue–torso cardiac electrophysiological model was integrated with a differential evolution (DE) algorithm. The forward model combined the Grandi atrial model and BPS2020 ventricular model, simulating action potential propagation via cellular automata and body surface ECGs via field point potentials. The inverse solution optimized 29 physiological parameters by minimizing the root-mean-square error between the simulated and clinical ECGs. The method was applied to 30 normal and 30 TWI cases to analyze the repolarization abnormalities. The study revealed that extracellular Ca^{2+} > 2.88 mmol/L and K^+ < 3.4 mmol/L in ventricular myocytes (Endo, M, Epi) induce TWI. Quantitative analysis identified specific 95% confidence intervals for ionic imbalances in three scenarios: Case 1 ($V_{Epi} > V_{Endo} > V_M$) with [Ca^{2+}] 2.60–3.30 mmol/L and [K^+] 1.9–4.7 mmol/L; Case 2 ($V_M > V_{Epi} > V_{Endo}$) with [Ca^{2+}] 2.36–3.68 mmol/L and [K^+] 3.13–4.07 mmol/L; and Case 3 ($V_{Epi} > V_M > V_{Endo}$) with [Ca^{2+}] 2.67–3.91 mmol/L and [K^+] 3.11–3.45 mmol/L. This approach enables cellular-scale mechanistic insights into TWI by quantifying ionic concentration changes. The framework supports the advancement of personalized cardiac diagnostics and drug development.

Keywords: T-wave inversion; differential evolution; cardiac electrophysiology; ECG inverse problem; ECG mechanisms

1. Introduction

Electrocardiogram (ECG) is one of the effective clinical aids in the diagnosis of cardiac diseases [1]. ECG records the changes in electrical activity produced by the heart with each heartbeat cycle. An ECG of a heartbeat cycle consists of four waveforms—namely, P, QRS, T and U waves with P-R and S-T ends and P-R and Q-T intervals [2]. In leads V3 to V6, the normal T-wave presents as an upright, low-amplitude, broad peak following the QRS complex. However, certain physiological and pathological conditions can cause the T-wave to invert. For example, in some young, healthy individuals, T-wave inversion may be a normal variation [3], while in other cases, it may signify underlying heart disease. In the early stages of myocardial infarction, T-wave inversion is an important predictor of recovery of cardiac function [4]. In patients with new coronary artery pneumonia, T-wave inversion can be a sign of early myocarditis [5]. In addition, T-wave inversion has been associated with the development of certain cardiac arrhythmias, such as ventricular fibrillation [6] and atrial fibrillation [7]. Therefore, understanding the relationship between T-wave inversion

Academic Editor: Maryam Ravan

Received: 9 April 2026
Revised: 4 May 2026
Accepted: 6 May 2026
Published: 9 May 2026

and myocardial electrical activity and investigating the mechanisms by which T-wave inversion arises are essential for diagnosing the pathophysiological mechanisms of various cardiovascular diseases and for safe drug therapy.

Methods for studying the relationship between ECG and electrical activity of the heart are classified into the forward problem of electrocardiology (FPE) and the inverse problem of electrocardiology (IPE). The FPE refers to the process of transforming the propagation of the electrical activity of the heart through the body tissues into the generation of surface ECG signals by means of computer simulations and numerical calculations [8]. Many studies have focused on the T-wave from the point of view of the FPE. In the early 1990s, Antzelevitch et al. identified a subpopulation of cells in canine ventricles with electrophysiological characteristics distinct from those of epicardial and endocardial cells, which were termed M cells [9–11]. Subsequently, researchers recorded the action potentials of these three types of ventricular myocytes using the single-cell Ten Tusscher–Noble–Noble–Panfilov 2006 (TNNP06) model [12] and the O'Hara–Rudy dynamic (ORd) model [13]. In 2024, Pascual-Sánchez et al. found that K^+ accumulation due to myocardial ischemia causes T-wave inversion [14]. These studies were based on simulation experiments based on existing medical findings, and their physiological parameters were determined in a stochastic manner, making it difficult to quantitatively describe the range of ions that cause T-wave abnormalities.

Unlike the FPE, the IPE attempts to restore the mechanisms by which cardiac activity is generated through inverse modeling [15]. In 2016, Barnes et al. proposed a regularization method based on robust generalized cross-validation to estimate epicardial potential distributions [16]. In 2020, Sahli Costabal et al. proposed a PINN method for inversely solving the activation time and conduction velocity [17]. In 2022, Tenderini et al. proposed a deep learning method to estimate epicardial potential fields by measuring the potentials at discrete points on the body surface [18]. These studies were often limited by the methodology or simple cardiac models, with the former ignoring the electrophysiological properties of the cardiac organ and the latter failing to specifically analyze pathological mechanisms at the ionic level. To fully appreciate the methodological positioning of our work, it is essential to consider the broader evolution of computational modeling paradigms. In related domains such as computer vision, there has been a profound transition from classical techniques to convolution-based models. Traditional methods often relied on handcrafted features and shallow models, which struggled with complex visual data and exhibited limited performance. Deep learning, particularly convolutional neural networks (CNNs), addressed these limitations by automatically learning rich, hierarchical, and high-level semantic features directly from data [19]. While recent CNN architectures have significantly improved the accuracy, they also inherently increased the computational complexity and resource demands. In the context of the IPE, adopting pure data-driven representation learning frameworks offers high scalability and generalization across diverse datasets. However, these models often function as "black boxes," making it difficult to extract biophysically meaningful parameters, especially specific ionic concentrations. Therefore, our approach strategically complements these deep learning trends: rather than relying solely on abstract feature representations, we couple a biophysically detailed forward model with a differential evolution optimization algorithm. This physics-based optimization ensures that the abstracted features remain strictly bounded by physiological laws, offering a level of mechanistic interpretability that pure convolutional models currently struggle to provide.

In this work, we combined the FPE and IPE methods to investigate the mechanism of T-wave inversion in ECG. We constructed a multiscale cardiac model using cellular automata to achieve forward mapping from electrophysiological parameters to the body

ECG. A differential evolutionary algorithm was used to optimize the model parameters, and the reverse mapping process was achieved by fitting real ECG data. Finally, the ion concentration parameters leading to T-wave inversion were quantitatively described at the cellular scale. While traditional IPE methods often rely on simplified geometric models or mathematical regularizations that ignore cellular electrophysiology, our proposed framework bridges this gap. By coupling the multiscale cellular automata forward model with the DE algorithm, this approach achieves a novel mapping from macroscopic body surface ECGs directly back to microscopic cellular ionic variations. This allows for the quantitative identification of specific pathological drivers, such as extracellular ion imbalances, which is a significant advancement over existing purely mathematical inverse solutions. This paper has four innovative points: a multiscale model links cellular physiology to body surface ECGs via cellular automata, the differential evolution algorithm inversely quantifies physiological parameters from ECG, the framework identifies specific ionic mechanisms underlying T-wave inversion, and extracellular Ca2+ and K+ imbalances in ventricular layers induce T-wave inversion.

2. Materials and Methods

In this paper, we constructed a multiscale cardiac electrophysiological model using the FPE method to realize the mapping relationship between the electrical activity of cardiomyocytes and the ECG, which divides the cardiac structure into three scales: cellular, tissue and torso. Subsequently, we used the IPE method to construct an ECG optimization model, which transforms the ECG inverse problem into an optimization problem, and with the help of an metaheuristic optimization algorithm to minimize the error between the simulated ECG and the actual ECG at the torso scale, and to obtain the optimal parameters of the cellular scale, so as to realize the solution of the ECG inverse problem. The whole process of the method is shown in Figure 1.

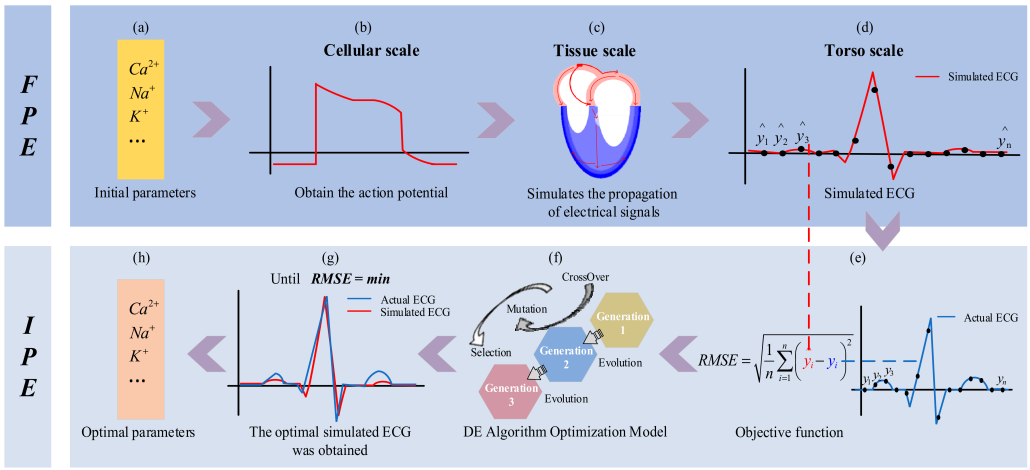

Figure 1. Overall experimental workflow diagram. In the FPE method, (**b**–**d**) describe the functions of the multiscale cardiac electrophysiological model. Moreover, (**a**) is the initial parameter, (**b**) is the acquisition of action potentials at the cellular scale, (**c**) is modeling action potential conduction at the tissue scale, and (**d**) is the formation of a simulated ECG at the torso scale. (**e**–**h**) Describe the IPE method. (**e**) The objective function is constructed using the root-mean-square error between the simulated ECG and the actual ECG. (**f**) Optimize the objective function using a differential evolutionary algorithm. In addition, (**g**) is the objective function minimized when the simulated ECG is closest to the actual ECG and (**h**) is the result of the IPE to obtain the optimal parameters.

2.1. Multiscale Cardiac Electrophysiological Model

In order to investigate the causes of T-wave inversion, it is first necessary to construct a multiscale cardiac electrophysiological model to simulate the human ECG. The ECG is the result of the propagation of the action potential through the heart. Cardiomyocytes are excited sequentially, generating action potentials (APs), which form a potential gradient difference between neighboring cells, leading to the generation of body surface potentials. The electrocardiogram reflects changes in the body surface potential over time. For this purpose, the cardiac structure is divided into three parts: cells, tissues and torso.

At the cellular scale, the action potentials of atrial and ventricular cells can be obtained. The models used in this process to simulate the action potentials of each cell are called cell-scale models. Electrophysiological models of cardiomyocytes include the Grandi atrial cell model [20], the Luo–Rudy ventricular cell model [21], the TNNP06 ventricular cell model [12], the ORd ventricular cell model [13], and the Bartolucci–Passini–Severi 2020 (BPS2020) ventricular cell model [22]. In this paper, we want to quantitatively explore the electrolyte abnormalities of the cardiac structure, and considering the stability of the models to different ion concentrations, the Grandi [20] atrial model and the BPS2020 [22] ventricular model have been selected for this paper. The schematic structure of the cardiomyocyte electrophysiological model is illustrated in Figure 2. The outermost layer of this structure is the cell membrane, on which the primary ion channels are distributed. The single-cell models employed in this study are all ion channel models based on the Hodgkin–Huxley (H-H) equation [23]. The H-H equation simulates the potential changes and ionic currents across the cardiomyocyte membrane by modeling the membrane and its internal components as an electrical circuit, as shown in Figure 3. In this circuit representation, resistors characterize the membrane's resistive properties, capacitors represent its capacitive characteristics, and current sources denote the activity and current contributions of ion channels.

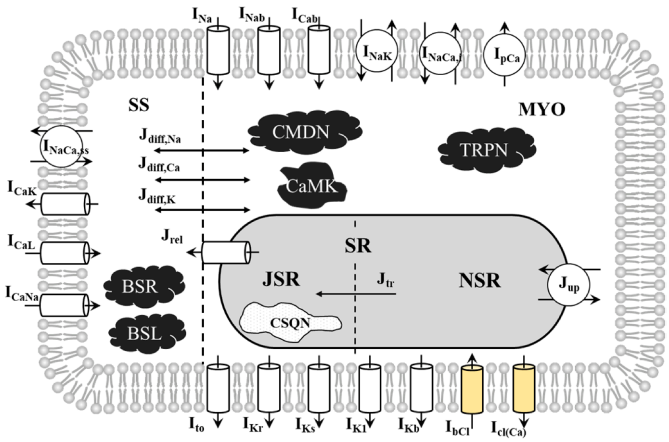

Figure 2. Schematic diagram of the human cardiac myocyte model. The model consists of four compartments: bulk myoplasm (MYO), junctional sarcoplasmic reticulum (JSR), network sarcoplasmic reticulum (NSR), and subspace (SS), resembling the area where the T-tubules are located. Currents into the myoplasm: the inward Na^+ current (I_{Na}), the transient outward K^+ current (I_{to}), the rapid and slow delayed rectifier K^+ currents (I_{Kr} and I_{Ks}, respectively), the inward rectifier K^+ current (I_{K1}), 75% of the $Na^+ - Ca^{2+}$ exchange current ($I_{NaCa,i}$), the $Na^+ - K^+$ pump current (I_{NaK}), background currents (I_{Nab}, I_{Cab}, and I_{Kb}), and the sarcolemmal Ca^{2+} pump current (I_{pCa}). Currents into subspace: the L-type Ca^{2+} current (I_{CaL}), 20% of the $Na^+ - Ca^{2+}$ exchange current ($I_{NaCa,ss}$). Ionic fluxes: Ca^{2+} through ryanodine receptor (J_{rel}), NSR to JSR Ca^{2+} translocation (J_{tr}), Ca^{2+} uptake into NSR via SERCA2a/PLB (J_{up}; PLB-phospholamban), and diffusion fluxes from subspace to myoplasm ($J_{diff,Na}$, $J_{diff,Ca}$, and $J_{diff,K}$).

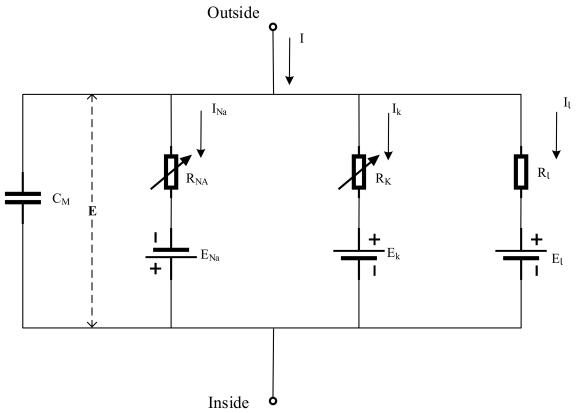

Figure 3. Based on experiments on squid axons, Hodgkin and Huxley proposed an equivalent circuit.

The equivalent equation for the cell membrane electrical activity [22] is as follows:

$$I = C_M \frac{dV}{dt} + I_i \tag{1}$$

where I is the total membrane current strength (inward current is negative); V is the membrane potential relative to its resting potential (depolarization is positive); C_M is the membrane capacitance per unit area (assumed to be a constant); t is the time; and I_i is the sum of the ionic current strengths (inward current is negative).

The atrial myocyte model used in this article is the Grandi model, which, unlike other atrial models, considers the concentration of chloride ion (Cl^-), the chloride ion background current (I_{Clb}), and the calcium-activated chloride current ($I_{Cl(Ca)}$), represented in the yellow ion channel in Figure 2. The expression for the total sum of ionic currents in the Grandi model can be derived from the atrial myocyte model with an equivalent cellular membrane circuit structure as shown in Figure 3, and it is as follows:

$$\begin{aligned} I_i = \quad & I_{Na} + I_{to} + I_{CaL} + I_{CaNa} + I_{Kr} + I_{Ks} + I_{K1} + I_{NaK} + I_{Nab} + \\ & I_{Kb} + I_{pCa} + I_{Cab} + I_{Kp} + I_{Clb} + I_{Cl(Ca)} \end{aligned} \tag{2}$$

In this paper, the ventricular myocyte model selected is the BPS2020 model. This model revises the Markov formula for I_{CaL} on the basis of the ORd model, and its main ion channels are the white-colored ones shown in Figure 2. When the ventricular myocyte model is equated to the cell membrane equivalent circuit structure presented in Figure 3, the expression for the total ionic current in the BPS2020 model is as follows:

$$\begin{aligned} I_i = \quad & I_{Na} + I_{to} + I_{CaL} + I_{NaL} + I_{CaNa} + I_{CaK} + I_{Kr} + I_{Ks} + I_{K1} + \\ & I_{NaCa\_i} + I_{NaCa\_ss} + I_{NaK} + I_{Nab} + I_{Kb} + I_{pCa} + I_{Cab} \end{aligned} \tag{3}$$

where I_i is the sum of the ion currents; I_{to} is the sum of the ion currents K^+ current; I_{CaL} is the Ca^{2+} current through the L-type Ca^{2+} channels; I_{CaNa} is the Na^+ current through the L-type calcium channels Na^+; I_{CaK} is the K^+ current through the L-type Ca_{2+} channel; I_{Kr} is the rapid delayed rectifier K^+ current; I_{Ks} is the slow delayed rectifier K^+ current; I_{K1} is the inward rectifier K^+ current; I_{NaCa_i} is the myoplasmic component of the Na^+/Ca^{2+} exchange current; I_{NaCa_ss} is the subspace component of the Na^+/Ca^{2+} exchange current; I_{NaK} is the $Na^+/K^+ - ATPase$ current; I_{Nab} is the Na^+ background current; I_{Cab} is the Ca^{2+} background current; I_{Kb} is the K^+ background current; I_{pCa} is the sarcolemmal Ca^{2+} pump current; I_{Kp} is the current of the K^+ platform; I_{Clb} is the Cl^- background current; and $I_{Cl(Ca)}$ is the Cl^- current that activates Ca^{2+}.

At the tissue scale, the process of action potential propagation through the interstitium between cardiac myocytes is simulated. Simulation methods include differential equation-based reaction–diffusion equation models and evolutionary rule-based cellular automata

(CA) models [24]. In this paper, a two-dimensional myocardial tissue model was developed using CA, which is a discrete dynamical system in time and space [25], and it is a simplified description of cardiac tissue, where each cell is updated to a new state depending on its previous state, as well as the states of its neighbors, and each cell has only a finite number of states, making the model computationally inexpensive [26]. The tissue model takes into account the four-chamber structure of the heart, the interventricular septum and the conduction tissue, where the ventricular myocytes are classified into subendocardial myocytes (Endo), mid-endocardial myocytes (M), and epicardial cells (Epi) based on the electrical heterogeneity of the ventricular myocytes. A two-dimensional cross-sectional structure of the heart was constructed based on these structural features, as shown in Figure 4.

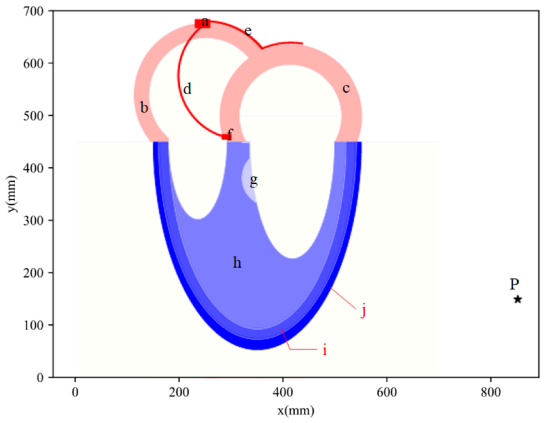

Figure 4. Simplified two-dimensional cross-sectional structure of the heart. The white area represents non-muscle cells in the cavity. The pale red area depicts atrial muscle cells (Art), with b and c referring to the left and right atria, respectively. The blue cells show ventricular muscle cells, while h, i, and j cells, respectively, represent the Endo cells, M cells, and Epi cells. The g cells represent interventricular septal cells. The conduction tissue cells are represented by deep red cells, with a, d, e, and f, respectively, representing the sinoatrial node, atrioventricular bundle, Bachmann bundle, and atrioventricular node. P indicates the electrode's position.

The cross-sectional structure of the two-dimensional heart is embedded in the 900 mm × 700 mm Cartesian coordinate system. Each coordinate (x, y) corresponds to a cardiomyocyte, and the entire coordinate system represents a complete CA system with a spatial resolution of 1 mm × 1 mm. The cellular status at a point (x, y) corresponding to a given time t is denoted by $\xi(x, y, t)$. Here, $\xi(x, y, t) \in \{0, 1, 2, 3, \ldots, n-1\}$, where n is the number of possible cellular states (an integer). Its value reflects the length of the action potential duration. When $\xi(x, y, t) = 0$, the cell is in the resting state. When $\xi(x, y, t) = 1$, the cell is in the excited state. When $\xi(x, y, t) \in \{2, 3, \ldots, n-1\}$, the cell is in a state of repolarization. The evolution rules of different cellular states under a CA algorithm are as follows:

$$\zeta(x, y, t+1) = \begin{cases} (\zeta(x, y, t) + 1) \bmod n, & \zeta(x, y, t) < n \\ 1, & \zeta(x, y, t) = 0 \text{ and } \theta(R) \geq \delta_{th} \\ 0, & \zeta(x, y, t) = 0 \text{ and } \theta(R) < \delta_{th} \end{cases} \quad (4)$$

where $\zeta(x, y, t)$ is the state of the cell at (x, y) at moment t; $\zeta(x, y, t+1)$ is the state of the cell at (x, y) at the next moment; R is the radius of the neighborhood of the cell; $\theta(R)$ denotes the number of neighbors in the excited state in the neighborhood of the domain radius R; and δ_{th} is the excitation threshold. The cellular states ζ are correlated with the transmembrane potentials of cardiomyocytes in Equation (1), with the time interval of time

step t set to 10 ms. A transmembrane potential value is sampled from the curve every 10 ms, and each discrete transmembrane potential value corresponds to a cellular state.

At the torso scale, myocardial electrical signals are converted into body surface potentials. The conduction of electrical signals in the heart generates a gradient of potential difference between neighboring cardiomyocytes, resulting in surface potentials. In this study, the field point potential calculation formula proposed by Zhu [27] was used to simulate cardiac activity by calculating the field point potential at time t. The formula for the field point potential is shown below:

$$\phi_p(t) = \frac{S_0}{4\pi} \sum_{i=1}^{N} \sum_{j=1}^{8} (V_i - V_{i,j}) \frac{\sigma_{in} \cos\theta_{i,j}}{\sigma_i r_{i,j}^2} \tag{5}$$

where P is the electrode location in Figure 4; $\phi_P(t)$ is the surface potential at time t when the electrode is located at position P; σ_i is the average conductivity from the $i-th$ myocardial cell to the P electrode; S_0 is a dimensionless constant; N is the total number of myocardial cells in the model; σ_{in} is the conductivity of the cytoplasm within the myocardial cells; V_i is the action potential of the $i-th$ myocardial cell in the model, which can be obtained from the equation; $V_{i,j}$ is the action potential of the $j-th$ neighbor of the $i-th$ myocardial cell in the model, which can be obtained from the equation; $r_{i,j}$ is the distance from the $j-th$ neighbor of the $i-th$ myocardial cell to the electric field that can be obtained from Figure 4 in the model; and $\theta_{i,j}$ is the angle between $\vec{ij}$ and $\vec{iP}$ that can be obtained from Figure 4.

As evident from our findings, the surface potential $\phi_P(t)$ varies over time, and the best estimate of the model parameters can be obtained through inverse solution accompanied by additional constraints.

2.2. ECG Optimization Model

In this study, an metaheuristic optimization algorithm is used to reconstruct the ECG inverse problem as an optimization problem. An optimization model was developed by the optimization algorithm to quantify the parameters of the multiscale model. The optimization problem consists of three elements: objective function, decision variables and constraints. The optimization steps are shown in Figure 5.

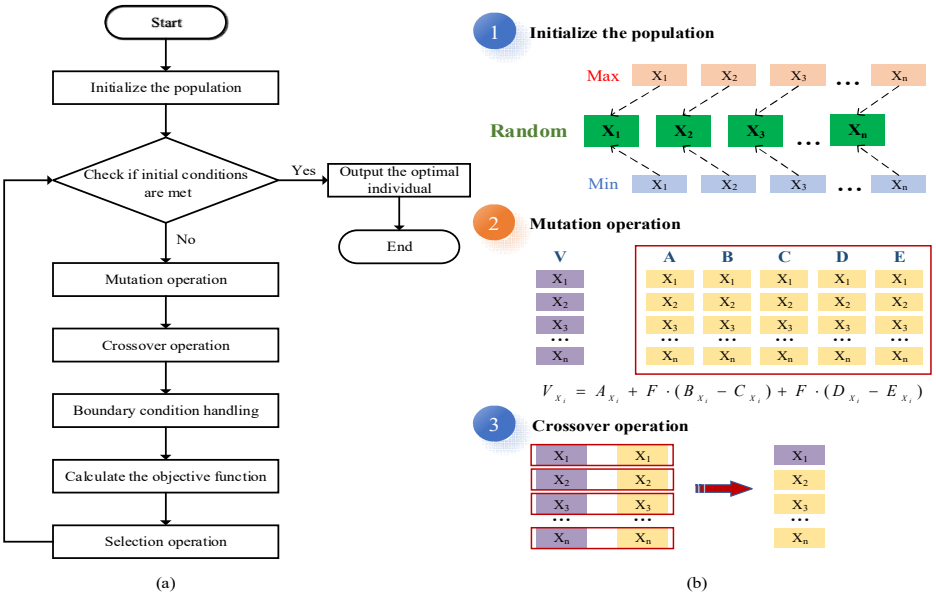

Figure 5. Specific steps of the optimization method: (**a**) is the flowchart of the optimization process using the differential evolution algorithm and (**b**) shows the key steps in the algorithm optimization process.

2.2.1. Objective Function

Objective Function: A function used to measure the degree of merit of a problem. The goal of an optimization problem is to maximize or minimize the value of the objective function.

The objective function in this paper is used to measure the difference between the ECG simulated by the multiscale electrophysiological model above and the real ECG. In this paper, the root-mean-square error (RMSE) is chosen as a measure of the simulated ECG versus the real ECG. Mathematically, because the RMSE squares the point-wise differences prior to averaging, errors are penalized quadratically rather than linearly. For instance, an error of 2 mV adds four times the penalty of a 1 mV error. This exponential sensitivity to large deviations ensures that the optimization algorithm strictly fits the critical peak amplitudes of the QRS complex and the repolarization phases of the T-wave, significantly reducing the likelihood of generating a flat or morphologically distorted simulated signal.

The formula for RMSE is as follows:

$$RMSE = \sqrt{\frac{1}{n}\sum_{i=1}^{n}\left(\hat{y}_i - y_i\right)^2} \tag{6}$$

where $\hat{y}_i$ is the model predicted value, which is, in this paper, the simulated body surface poten-tial; y_i is the actual observed value, which is, in this paper, the real body surface potential; and n is the number of samples.

From the above equation, we can know that $\hat{y}_i = \phi_P(t)$, the real ECG also changes with time, then the real body surface potential at the moment *of t* is $\varphi(t)$, which is brought into the equation to obtain the objective function of this paper, as shown in the following equation:

$$RMSE = \sqrt{\frac{1}{T}\sum_{t=0}^{T}\left(\phi_P(t) - \varphi(t)\right)^2} \tag{7}$$

where $\phi_P(t)$ is the simulated body surface potential at moment t of equation and $\varphi(t)$ is the real body surface potential at moment t of the real.

2.2.2. Decision Variables

Decision variables are the variables that need to be determined in the optimization problem and their values will affect the results of the objective function. From the equation, the value of the RMSE is affected by equation $\phi_P(t)$, while $\phi_P(t)$ is affected by the parameters of the multiscale cardiac electrophysiology model. In this paper, the parameters of the multiscale cardiac electrophysiology model that have physical significance are chosen as the decision variables of the optimization model. The decision variables as model inputs and body surface potentials as outputs are expressed as a functional form, then the parameters can be expressed as x_i, as shown in Table 1, which shows the variable meanings of the selected model parameters, and then Equation (5) can be expressed as follows:

$$\phi_P(t) = f(x_1, x_2, \ldots, x_{29}) \tag{8}$$

Table 1. Decision variables for the ECG optimization model.

Decision Variables	Variable Name	Variable Meaning
x_1	S_0	Dimensionless constant
x_2	δ_{in}	Intracellular fluid conductivity
x_3	δ_i	Average conductivity from the *i-th* myocardial cell to the p electrode
x_4	R_art	Speed of signal propagation in the atrium

Table 1. *Cont.*

Decision Variables	Variable Name	Variable Meaning
x_5	R_sn	Speed of signal propagation in the sinoatrial node
x_6	R_bb	Speed of signal propagation in the Bachmann bundle
x_7	Ven_CL	The pacing cycle length of the ventricle
x_8	$Endo\_Na_o$	Extracellular Na^+ concentration in the Endo cells
x_9	$Endo\_Ca_o$	Extracellular Ca^{2+} concentration in the Endo cells
x_{10}	$Endo\_K_o$	Extracellular K^+ concentration in the Endo cells
x_{11}	Epi_Na_o	Extracellular Na^+ concentration in the Epi cells
x_{12}	Epi_Ca_o	Extracellular Ca^{2+} concentration in the Epi cells
x_{13}	Epi_K_o	Extracellular K^+ concentration in the Epi cells
x_{14}	M_Na_o	Extracellular Na^+ concentration in the M cells
x_{15}	M_Ca_o	Extracellular Ca^{2+} concentration in the M cells
x_{16}	M_K_o	Extracellular K^+ concentration in the M cells
x_{17}	Ven_Temp	Ventricular ambient temperature
x_{18}	Ven_Cell_L	Ventricular myocyte length
x_{19}	Ven_Cell_R	Radius of ventricular myocytes
x_{20}	Art_CL	Pacing cycle length of atrium
x_{21}	Art_Cl_{in}	Atrial intracellular fluid Cl^- concentration
x_{22}	Art_Cl_o	Atrial extracellular fluid Cl^- concentration
x_{23}	Art_K_o	Atrial extracellular fluid K^+ concentration
x_{24}	Art_Na_o	Atrial extracellular fluid Na^+ concentration
x_{25}	Art_Ca_o	Atrial intracellular fluid Ca^{2+} concentration
x_{26}	Art_Mg_{in}	Atrial intracellular fluid Mg^{2+} concentration
x_{27}	Art_Temp	Atrial ambient temperature
x_{28}	Art_Cell_L	Atrial cell length
x_{29}	Art_Cell_R	Atrial cell radius

2.2.3. Constraints

In the process of solving the ECG inverse problem, setting constraints is a key step to ensuring the reasonableness and effectiveness of the optimization model results. Its main purpose is to limit the value range of the decision variables, so that the solution results are in line with the basic laws of cardiac physiology and electrical conduction, and at the same time, reflect the characteristics of the electrical activities of the heart under normal physiological conditions.

From the point of view of cardiac physiology, the electrical activity of the heart depends on the transmembrane transport of various ions and the physiological properties of cardiomyocytes, and these physiological processes have strict requirements on the value ranges of the relevant parameters. For example, abnormal changes in the ion concentration may lead to disturbances in cardiac electrical activity, so the ion concentration parameter in the decision variable must be limited to a reasonable interval to ensure that the electrical activity simulated by the model is consistent with the real physiological situation.

In order to achieve the above objectives, two main methods of constraint setting are used in this paper.

Physical constraints: To ensure that the solution of the cardiac inverse problem conforms to the physical laws of cardiac physiology and electrical conduction, a reasonable range of values is set for each decision variable. Specifically, the decision variables need to satisfy the following:

$$x_i^{\min} \leq x_i \leq x_i^{\max} \tag{9}$$

where x_i represents the first i decision variable, while x_i^{min} and x_i^{max} represent the minimum and maximum values it can take, respectively. In this way, the range of variation of each

parameter is effectively limited to avoid parameter values that do not correspond to physiological reality.

Similarity constraints: Consider that under normal physiological conditions, the three main cells in the ventricle (Epi, M, and Endo) have similar distributions of electrical activity. Based on this, this physiological feature is reflected by constraining the solution of the ventricular myocyte parameters to be close within a certain range, which makes the optimization results more accurately reflect the characteristics of normal cardiac electrical activity.

2.2.4. Solution Methods

Common methods for solving optimization problems include the classical genetic algorithm (GA) [28], differential evolutionary (DE) algorithm [29] and the latest sparrow search algorithm (SSA) [30]. The differential evolutionary algorithm [29] proposed by Rainer Stron and Kenneth Price is used in this study. Compared with the GA, the DE has stronger robustness, faster convergence and stronger global optimization search capability [31]. Compared with the SSA, the DE has faster solution speed and better ability to jump out of the local optimum [32]. The DE generates temporary individuals based on the individual dissimilarity within the population and then randomly recombines to achieve population evolution. It mainly includes initializing the population, mutation operation, crossover operation and so on. The specific evolution process is described as follows:

1. Initializing the population

The DE algorithm produces a certain number of initial populations by encoding them in real numbers. Randomly producing N D-dimensional vectors M as initial populations, then each individual can be denoted as $x_i(G) = (x_{i1}(G), x_{i2}(G), \ldots, x_{iD}(G))$. The initial population is produced in $[x_{\min}, x_{\max}]$ and the initial fitness of each individual is obtained by certain initialization strategy, where M is the component of D-dimensional vector, N is the number of populations, and $x_i(G)$ is the *ith* individual. The initialization strategy is shown in Equation (10):

$$x_{iD} = x_{\min} + rand_{\mathrm{j}}(0,1) * (x_{\max} + x_{\min}) \tag{10}$$

where G represents the G th generation; $x_{\min}$ represents the minimum value of the search space; $x_{\max}$ represents the maximum value of the search space; and $rand_j(0,1)$ is a random number that satisfies the normal distribution in (0,1).

2. Mutation operation

The mutation operation produces new individuals by mutating individuals in the current population. Performing differential mutation on each individual in the current population x_i^G produces the mutation vector V_i^G, the choice of mutation strategy is one of the keys of the differential evolution algorithm, and different mutation strategies will have an impact on the performance of the algorithm. The following are three common variation strategies:

(a) The "rand/1" strategy: This is one of the most commonly used mutation strategies. In this strategy, three different individuals are randomly selected and then new individuals are generated by linear combination. The formula is expressed as follows:

$$V_i^G = x_i^G + F \cdot \left(x_{r2}^G - x_{r3}^G\right) \tag{11}$$

(b) The "best/1" strategy: In this strategy, the best individual in the current population is used as the benchmark individual, and another randomly selected individual is linearly combined to generate a new individual. The formula is given as follows:

$$V_i^G = x_{best}^G + F \cdot (x_{r1}^G - x_{r2}^G) \tag{12}$$

(c) The "rand/2" strategy: The strategy is to select two different individuals to be linearly combined to generate a new individual. The formula is given as follows:

$$V_i^G = x_{r1}^G + F \cdot (x_{r2}^G - x_{r3}^G) + F \cdot (x_{r4}^G - x_{r5}^G) \tag{13}$$

where $r1$, $r2$, $r3$, $r4$ and $r5$ are mutually exclusive integers randomly formed within [1,M] and $r1 \neq r2 \neq r3 \neq r4 \neq r5$; x_{best}^G is the vector of individuals with the lowest fitness in generation G; x_i^G is the individual before the mutation; V_i^G is the individual after the mutation; and F is the scaling factor, which is a positive control parameter on the scaled difference vector.

3. Crossover operation

The crossover operation $r1, r2, r3, r4$ is carried out between the mutant individuals (V_i^G) and the current individuals (x_{r1}^G) for generating new offspring individuals (U_i^G) to enhance the population diversity. The crossover strategy is calculated as shown in the following equation:

$$U_i^G = \begin{cases} V_i^G & if\left(rand_j(0,1) \leq CR_i\right) \; or \; (j = j_{rand}, j = 1,2,3,\ldots,D) \\ x_i^G & otherwise \end{cases} \tag{14}$$

where $rand_j(0,1)$ is a random number satisfying a normal distribution within (0,1); j_{rand} is a randomly chosen integer on [1,D]; and CR_i is the crossover probability corresponding to individual x_i.

3. Results

3.1. Results of the FPE

3.1.1. Results of the FPE Simulation of a Normal ECG

According to the experimental data, the pacing cycle length of the Grandi atrial model and the BPS2020 ventricular model was set at 1000 ms, and the sampling frequency was 100 Hz. In each model, the intracellular Cl^- concentration was set at 15 mmol/L, the extracellular Cl^- concentration was set at 150 mmol/L, the extracellular K^+ concentration was set at 5.4 mmol/L, and the extracellular Na^+ concentration was set at 140 mmol/L. The extracellular Ca^{2+} concentration was 1.8 mmol/L, and the intracellular Mg^{2+} concentration was set to 1 mmol/L. The field point coordinates P (850,150) corresponded to the position of the V6 lead in the 12-lead ECG.

The point-line diagram of the action potential variation over time obtained is shown in Figure 6.

By applying the cellular states from Figure 6 and their corresponding action potential values at time t to Equations (5) and (6), and with a propagation velocity of the electrical signal of 0.05 m/s in the sinoatrial node, 1 m/s in the atria, 1.7 m/s in the Bachmann bundle, and 1.7 m/s in the internodal pathways, Figures 7 and 8 are obtained.

Table 2 compares the simulated ECG in Figure 8 with the clinical normal ECG metrics [33], verifying the validity of the model's mapping from electrophysiological parameters to the body surface ECG.

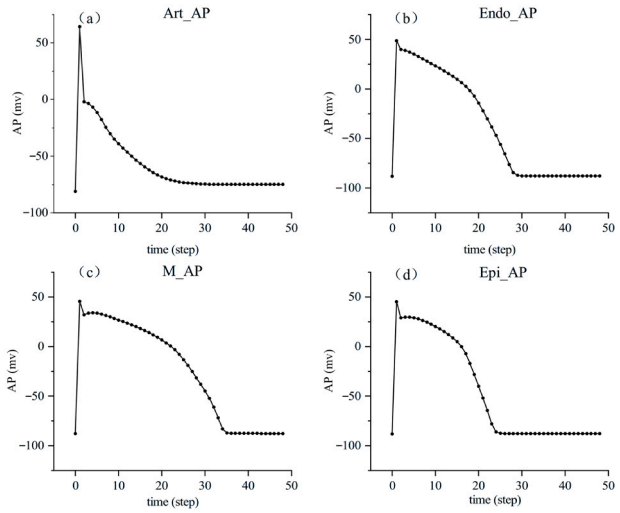

Figure 6. Simulation of atrial and ventricular action potentials. The x-axis is the time (step) and the y-axis is the action potential voltage in millivolts (mV): (**a**–**d**) depict the temporal variation of action potential for Art cells, Endo cells, M cells, and Epi cells in the heart during the cardiac cycle.

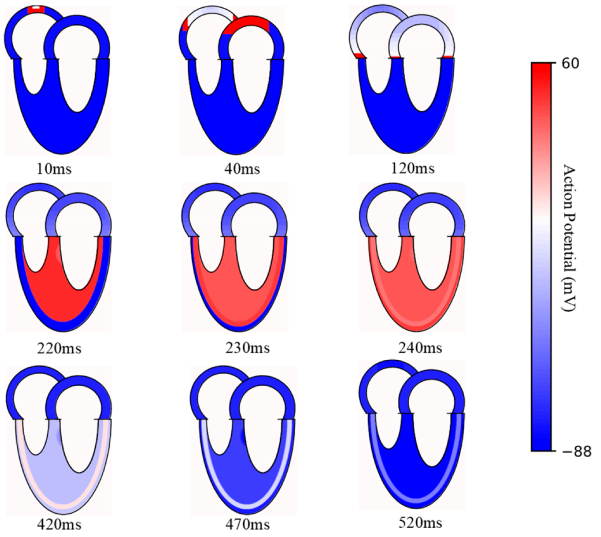

Figure 7. Propagation of electrical signals in the heart. The dark blue color in the figure represents the resting transmembrane potential and the dark red color represents the transmembrane potential after depolarization. The other colors in the figure represent the transmembrane potential during repolarization.

Table 2. Comparison of the simulated ECG with clinical normal ECG indices.

ECG Feature	Action	Simulated ECG (ms)	Normal Duration (ms)
P wave	Depolarization of the right and left atria	80	80–110
PR interval	Onset of atrial depolarization (P-wave) to onset of ventricular depolarization (start of QRS complex)	150	120–200
Q wave	First negative deflection after the P-wave, if present	20	<40
QRS complex	Right and left ventricular depolarization	70	70–100
QT interval	Duration of ventricular depolarization and repolarization; measured from the beginning of the QRS complex to end of T-wave	330	<460

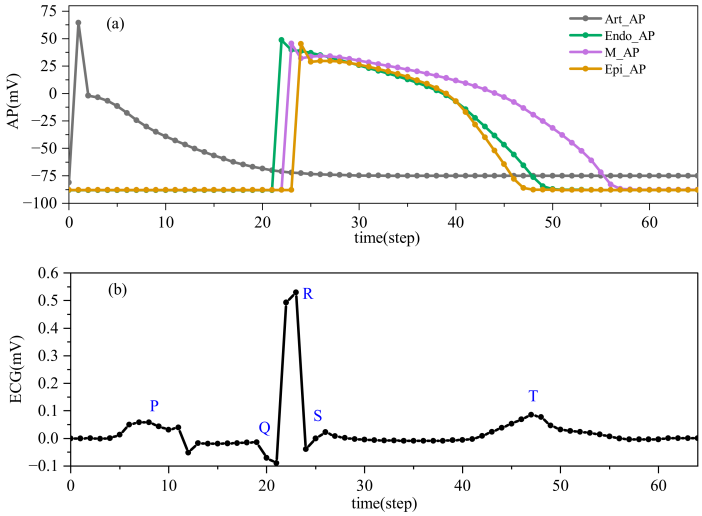

Figure 8. Simulated ECG under normal electrical activity. The x-axis is the time (Step) and the y-axis is the potential (mV). (**a**) Curve of the transmembrane potential of atrial and ventricular cells over time. (**b**) ECG waveform under normal electrical activity.

3.1.2. Results of the FPE Simulation of a T-Wave Inversion ECG

To evaluate the stability of the multiscale model in abnormal environments, we first validated multiple electrolyte abnormalities. For Ca^{2+}, the extracellular Ca^{2+} concentrations were set at 0.5 mmol/L, 1.0 mmol/L, 1.5 mmol/L, 2.0 mmol/L, 2.5 mmol/L, and 3.0 mmol/L, respectively, and the action potential time courses (APDs) at different concentrations were investigated, as shown in Figure 9a,b. For K^+, the ECG changes at $0.9G_k$, $0.8G_k$, $0.7G_k$, $0.6G_k$, and $0.5G_k$ were investigated by adjusting the maximum conductance G_k of the I_K channel to simulate the K^+ channel block, as shown in Figure 9c,d. For Na^+, the ECG changes at $0.9G_{Na}$, $0.8G_{Na}$, $0.7G_{Na}$, $0.6G_{Na}$, and $0.5G_{Na}$ were investigated by adjusting the maximum conductance G_{Na} of the fast sodium current (I_{Na}) to simulate the blockage of the Na^+ channel, as shown in Figure 9e–g.

Afterwards, the parameters were set according to the pathology report of Moon et al. [34], in which the pacing cycle length of the Grandi atrial model and the BPS2020 ventricular model was set at 1000 ms and the sampling frequency at 100 Hz. The intracellular Cl^- concentration was 15 mmol/L, the extracellular Cl^- concentration was 150 mmol/L, the extracellular K^+ concentration was 2.1 mmol/L, the extracellular Na^+ concentration was 140 mmol/L, the extracellular Ca^{2+} concentration was 0.72 mmol/L, the intracellular Mg^{2+} concentration was set to 1 mmol/L, the coordinates of the field point, P (541,200), corresponded to the position of V3 lead in the 12-lead ECG, and the final ECG of T-wave inversion was simulated, as shown Figure 10, which shows the T-wave inversion relationship between the action potentials of cardiomyocytes and the ECG under pathological conditions.

3.2. Results of the IPE

3.2.1. Results of the IPE Solving Normal ECGs

Clinical ECG data were obtained from the SID medical database, including 30 normal ECGs and 30 cases of T-wave inversion. Prior to interpolation, the raw signals underwent standard digital signal preprocessing to account for instrumental and environmental noise. Specifically, a median filter was utilized to remove the baseline wander, and a bandpass filter was applied to eliminate high-frequency noise and powerline interference. Following noise reduction, the raw data were sampled at 500 Hz and then resampled to 100 Hz using cubic spline interpolation to ensure consistency with the temporal resolution of the

multiscale model. Normal V6-lead heartbeat data from 30 randomly selected individuals were used in the ECG optimization model (built from Equation (16)). We compared the DE, NSGA2 and SSA algorithms to optimize the multiscale cardiac model. The differential evolution algorithm was finally chosen.

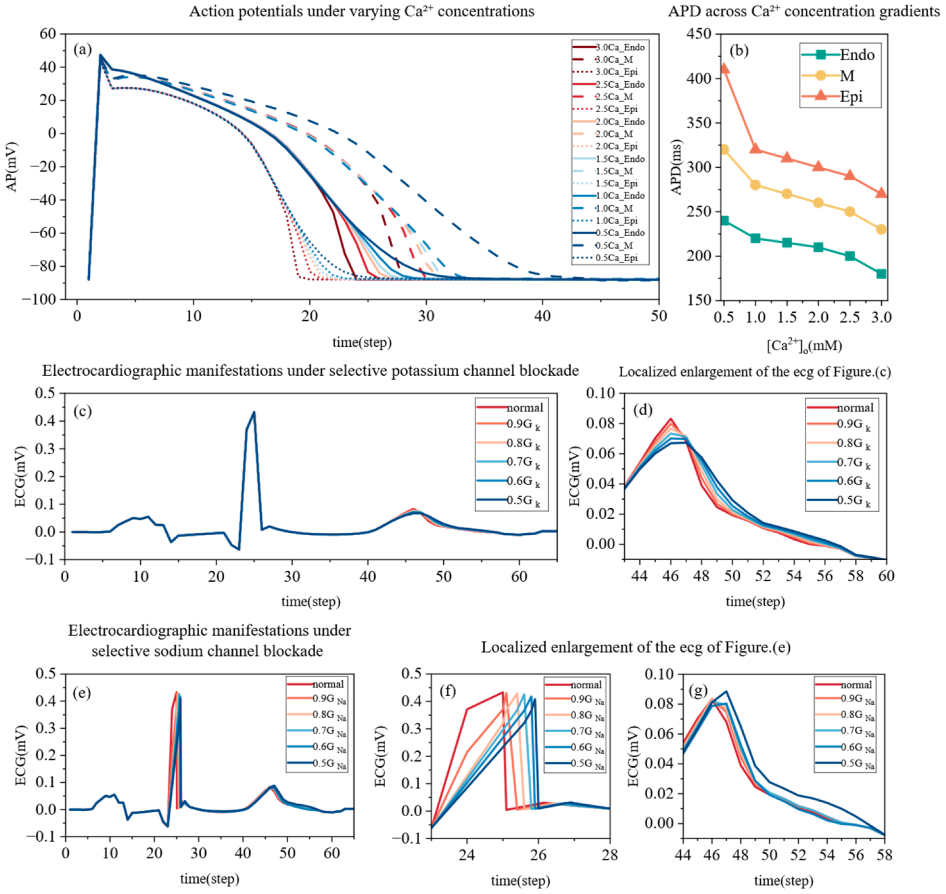

Figure 9. ECG under simulated electrolyte abnormalities: (**a**) is the action potential of ventricular cells at different Ca^{2+} concentrations, (**b**) is the APD of ventricular cells at different Ca^{2+} concentrations, (**c**) is the electrocardiographic performance in the case of selective potassium channel blockade, (**d**) is a local enlargement of the electrocardiographic performance of (**c**), and (**e**) is the electrocardiographic performance in the case of selective sodium channel blockade. ECG performance: (**f**) and (**g**) are local enlargements of the (**e**) ECG.

To ensure that the differential evolution algorithm could explore parameter spaces corresponding to both normal physiological states and severe pathological conditions, the global search boundaries (x_i^{min} and x_i^{max}) were defined to cover extreme clinical limits [20,22,35–37]. For example, the boundaries for extracellular K^+ were set between 1.5 and 8.0 mmol/L to accommodate severe hypokalemia and hyperkalemia, while the extracellular Ca^+ bounds were set between 0.5 and 4.0 mmol/L. The specific initial boundary conditions for key ionic decision variables are explicitly listed in Table 3.

Table 3. Explicit optimization boundary conditions for key ionic parameters.

Decision Variables	x_i^{min}	x_i^{max}
x_{10}, x_{13}, x_{16}, x_{23}	1.5	8.0
x_9, x_{12}, x_{15}, x_{25}	0.5	4.0
x_8, x_{11}, x_{14}, x_{24}	130	150
x_{28}	50	160
x_{29}	5	16

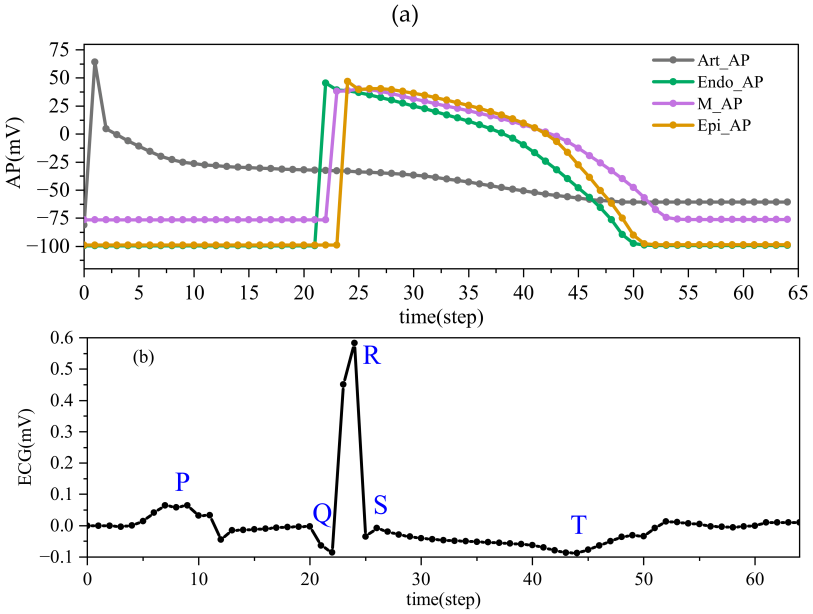

Figure 10. Simulated ECG under abnormal electrical activity. The x-axis is the time (Step) and the y-axis is the potential (mV). (**a**) Curve of the transmembrane potential of atrial and ventricular cells over time. (**b**) ECG waveform under abnormal electrical activity.

According to the similarity constraint, the Na^+ concentration differences among the three types of ventricular cells were within 5 mmol/L, the K^+ concentration differences within 2 mmol/L, and the Ca^+ concentration differences within 0.5 mmol/L, as shown in Equation (15):

$$\begin{cases} |x_8 - x_{11}| < 5\,, & |x_{11} - x_{14}| < 5\,, & |x_8 - x_{14}| < 5 \\ |x_9 - x_{12}| < 0.5\,, & |x_{12} - x_{15}| < 0.5\,, & |x_9 - x_{12}| < 0.5 \\ |x_{10} - x_{13}| < 2\,, & |x_{13} - x_{16}| < 2\,, & |x_{10} - x_{16}| < 2 \end{cases} \tag{15}$$

Combining the above Equations (7)–(9) and (15), the value of the RMSE as an objective function is denoted by y. The optimization model of ECG is established as follows:

$$\min y = \sqrt{\frac{1}{T}\sum_{t=0}^{T}\left(f(x_1, x_2, \ldots, x_{29}) - \varphi(t)\right)^2}\,, x_i^{\min} \le x_i \le x_i^{\max} i = 1, 2, 3, \ldots, 29$$
$$s.t \begin{cases} |x_8 - x_{11}| < 5\,, & |x_{11} - x_{14}| < 5\,, & |x_8 - x_{14}| < 5 \\ |x_9 - x_{12}| < 0.5\,, & |x_{12} - x_{15}| < 0.5\,, & |x_9 - x_{12}| < 0.5 \\ |x_{10} - x_{13}| < 2\,, & |x_{13} - x_{16}| < 2\,, & |x_{10} - x_{16}| < 2 \\ \text{When inverse optimizing normal ECG} \end{cases} \tag{16}$$

When the differential evolutionary algorithm was used to optimize the model, the mutation strategy was "best/1", the F scaling factor in Equation (13) was set to 0.5, the CR crossover probability in Equation (15) was set to 0.5, the population size N was 30, and the number of iterations was 120. When the NSGA2 and SSA algorithms are used, the population size N weas 30 and the total number of iterations was also 120. The optimization results for 30 groups of normal individuals are shown in Figure 11.

To quantitatively describe the parameter ranges of a normal ECG, we counted the optimal parameters for 30 groups of individuals and plotted box plots for 29 parameters. To address the problem that some of the parameter ranges were too large, we normalized them and displayed them in Figure 12. The size of the box represents the degree of dispersion, with larger boxes indicating higher variability and smaller boxes indicating more stable variables.

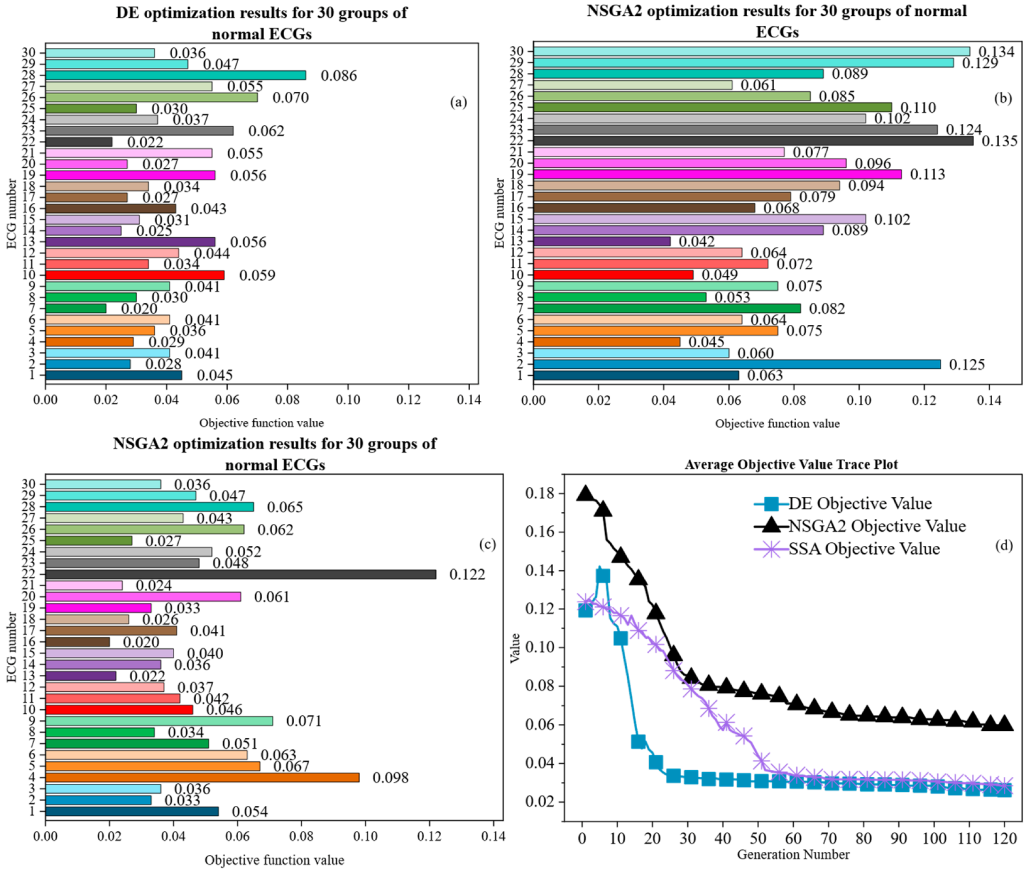

Figure 11. (**a**–**c**) The optimization results of the DE, NSGA2 and SSA algorithms for 30 groups of individuals, respectively. The x-axis reflects the RMSE value defined in Equation (8), and the y-axis represents the sequence number of 30 ECGs. Moreover, (**d**) is the average objective function convergence curve for 30 groups of individuals. The x-axis is the number of iterations and the y-axis is the objective function value.

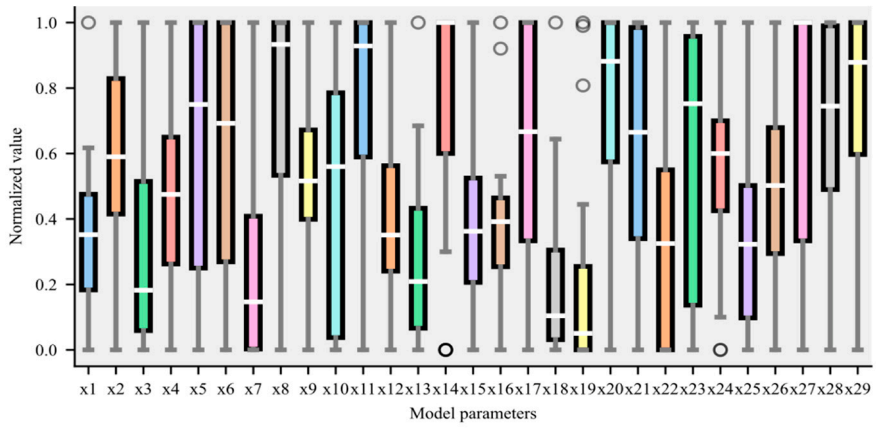

Figure 12. Box plot of the optimized 29 parameters of a multiscale cardiac electrophysiological model. The x-axis is the 29 parameters, and the y-axis is the normalized optimal value of the parameter. The white line in the box represents the median, and the empty points represent the outliers.

The optimal parameters of 30 normal ECGs were statistically analyzed using Figure 12. We eliminated the outliers among the abnormal values and recorded the maximum and minimum values of each parameter to derive the range of parameters for normal ECGs, as shown in Table 4.

Table 4. Normal ranges of values for the 29 parameters of the multiscale model.

	Range of Values	Parameters	Range of Values	Parameters	Range of Values
x_1	[2.42, 10.0]	x_{11}	[134, 145]	x_{21}	[9.96, 20]
x_2	[0.48, 0.95]	x_{12}	[1.4, 2.89]	x_{22}	[139, 159]
x_3	[1.02, 1.86]	x_{13}	[3.40, 5.98]	x_{23}	[3.40, 5.58]
x_4	[0.5, 1.2]	x_{14}	[135, 144]	x_{24}	[135, 145]
x_5	[0.01, 0.06]	x_{15}	[1.60, 2.58]	x_{25}	[1.4, 2.5]
x_6	[0.7, 2]	x_{16}	[3.50, 5.87]	x_{26}	[0.6, 1.47]
x_7	[400, 1000]	x_{17}	[35.9, 37.9]	x_{27}	[35.9, 38.85]
x_8	[135, 145]	x_{18}	[0.009, 0.013]	x_{28}	[50, 150]
x_9	[1.5, 2.7]	x_{19}	[0.0009, 0.0014]	x_{29}	[5, 12]
x_{10}	[3.30, 5.96]	x_{20}	[870, 1000]		

The ECG was simulated using a multiscale cardiac electrophysiology model (described in Section 2.1) with 30 sets of optimal parameters, and Figure 13 was generated to compare the optimized ECG with the actual ECG, which was in general agreement with the actual ECG.

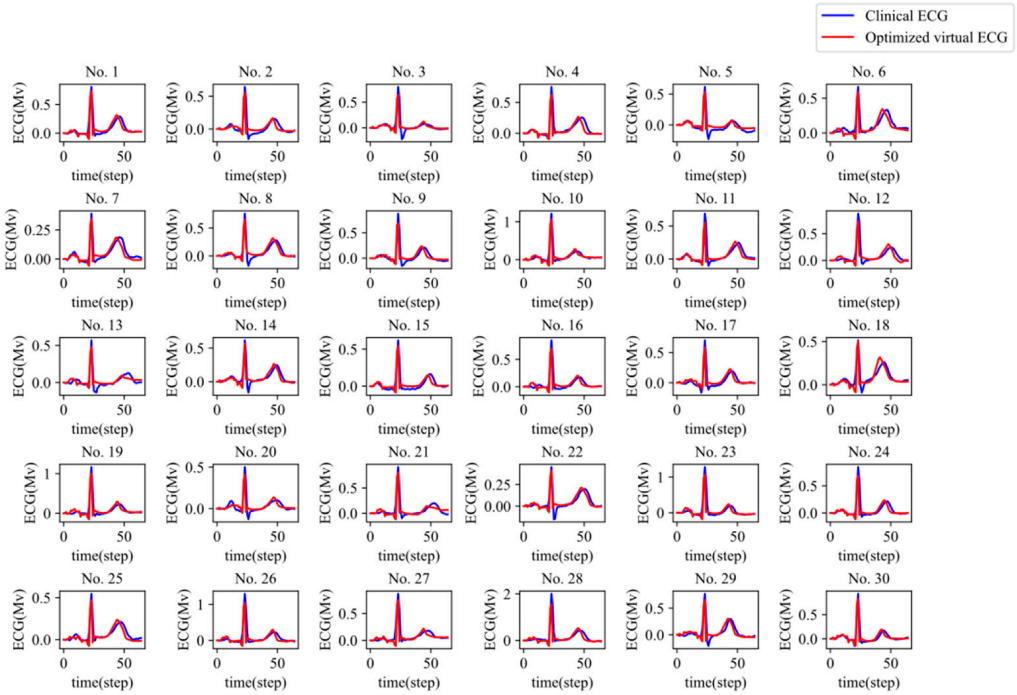

Figure 13. The comparison between the optimized ECG and the actual ECG recorded in the clinic. The x-axis of the figure represents the time (steps), and the y-axis represents the potential (mV). The blue curve in the figure depicts the trend over time of clinically normal ECGs, while the red curve represents the trend over time of the optimized ECG.

Table 5 compares this paper with several existing cardiac inverse methods. We solved for parameters at the smallest level of the multiscale cardiac model, which means that inverse solutions at other levels, such as tissue or torso scales, can be achieved in the same way.

3.2.2. Results of the IPE Solving T-Wave Inverted ECGs

Similarly, we randomly selected 30 V6 lead heartbeat data with T-wave inversion from Sid Medical. We applied the same optimization model parameters as in Section 3.2.1. The optimization convergence plot is shown Figure 14.

Table 5. Comparison with existing ECG inverse solution methods

IPE Methodology	Solution Objective	Scale	Bibliography
Regularization method based on robust generalized cross-validation	Surface and body surface potential distribution	Torso level	Barnes et al., 2016 [16]
Physics-informed neural networks	Activation time and conduction velocity	Tissue level	Sahli Costabal et al., 2020 [17]
Space–time reduced basis deep neural network	Epicardial and body surface potential distribution	Torso level	Tenderini et al., 2022 [18]
Multiscale model—differential evolutionary algorithm for inverse solution of T-wave inversion in electrocardiography	Cell-scale electrolyte concentrations	Cellular level	This paper

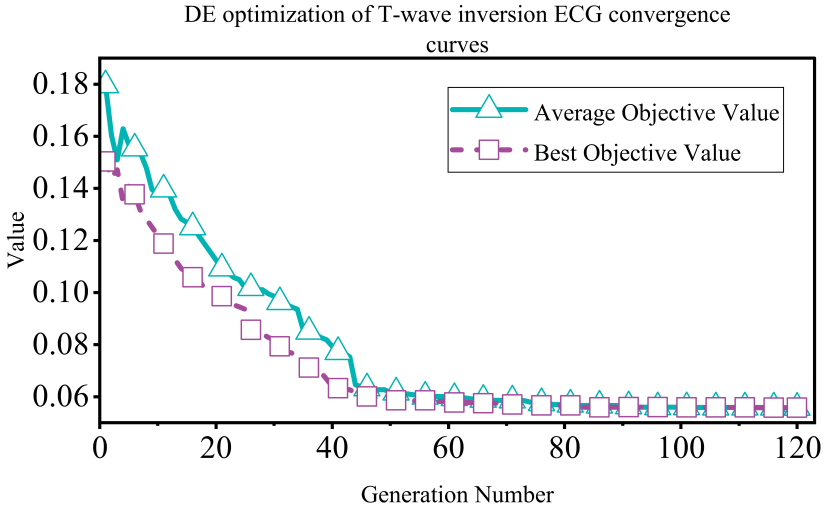

Figure 14. Convergence curve of the objective function of the DE algorithm for optimizing a T-wave inverted ECG. The x-axis is the number of iterations and the y-axis is the objective function value. The green line represents the average objective function value curve for 30 individuals per generation, and the purple line represents the minimum objective function value curve for 30 individuals per generation.

Figure 15 quantifies the optimization results for 30 groups of T-wave inversions. Group 6 has the smallest error of 0.023, while group 26 has the largest error of 0.184. Root-mean-square errors below 0.2 were observed in all 30 ECGs.

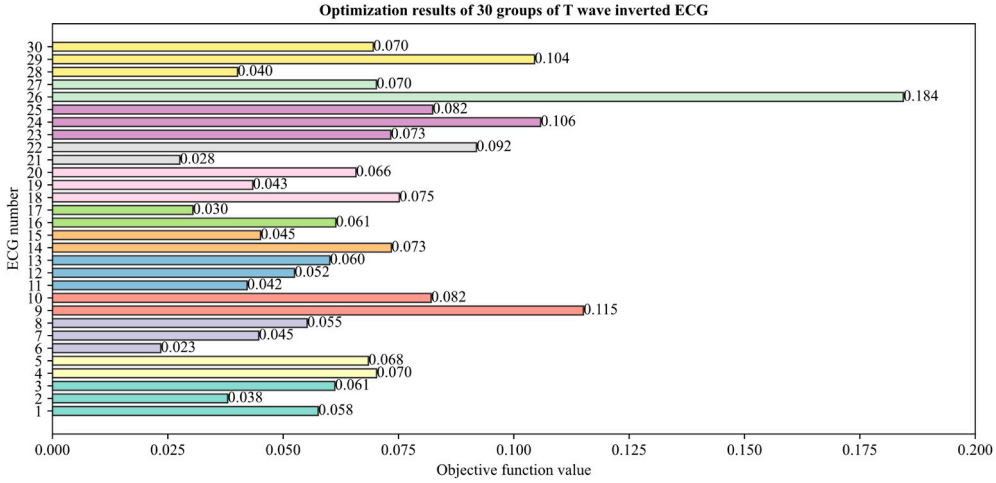

Figure 15. The x-axis represents the RMSE value defined in Equation (8) and the y-axis represents the sequence number of 30 T-wave inverted ECGs.

The T-wave inverted ECG was simulated using a multiscale cardiac electrophysiological model (described in Section 2.1) with 30 sets of optimal parameters, generating Figure 16, which is a comparison of the optimized T-wave inverted ECG with the real T-wave reversed ECG.

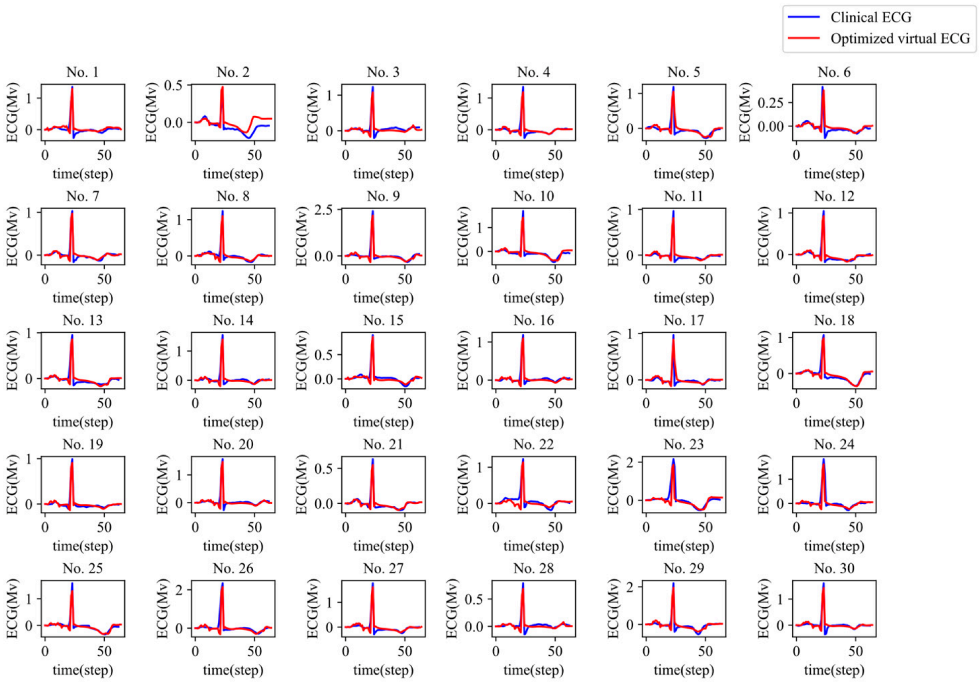

Figure 16. Optimized T-wave inverted ECG versus clinically recorded actual T-wave inverted ECG. The x-axis represents the time (steps) and the y-axis represents the potential (mV). The blue curve represents the clinically observed T-wave inverted ECG over time, and the red curve represents the optimized ECG over time.

3.3. Results of Quantitative Analysis of T-Wave Inversion Mechanism

The inverse solution parameters of 30 sets of T-wave inverted individuals were set at the cellular scale, and the action potential changes of ventricular myocytes during repolarization were observed to obtain the three scenarios of inversion of the generated T-wave, as shown in Figure 17. Comparing with the Figure 8a repolarization phase normally $V_M > V_{Endo} > V_{Epi}$, Epi is the first to complete repolarization, followed by Endo, and finally, M cells. Figure 17a shows the first abnormal situation (AS1), the repolarization phase $V_{Epi} > V_{Endo} > V_M$. Figure 17b shows the second anomaly (AS2), repolarization phase $V_M > V_{Epi} > V_{Endo}$. Figure 17c shows the third anomaly (AS3), repolarization phase $V_{Epi} > V_M > V_{Endo}$.

Quantitative analysis of the inverse solution parameters of 30 groups of abnormal individuals against Table 2 shows that these abnormalities were caused by abnormal Ca^{2+} and K^+ concentrations in the 29 ventricular parameters, while all the other parameters were within the normal range of Table 2, the statistics of which are shown in Figure 18. The solid points are the values of the K^+ concentration and the Ca^{2+} concentration of the three types of cells of the ventricular muscle, taking the values of the concentrations, which are outside the shading as abnormal values and inside the shading as normal values. Figure 18a–c depict the values of the K^+ and Ca^{2+} concentrations in the three types of ventricular muscle cells for the first, second, and third abnormalities, respectively, corresponding to Figure 17a–c.

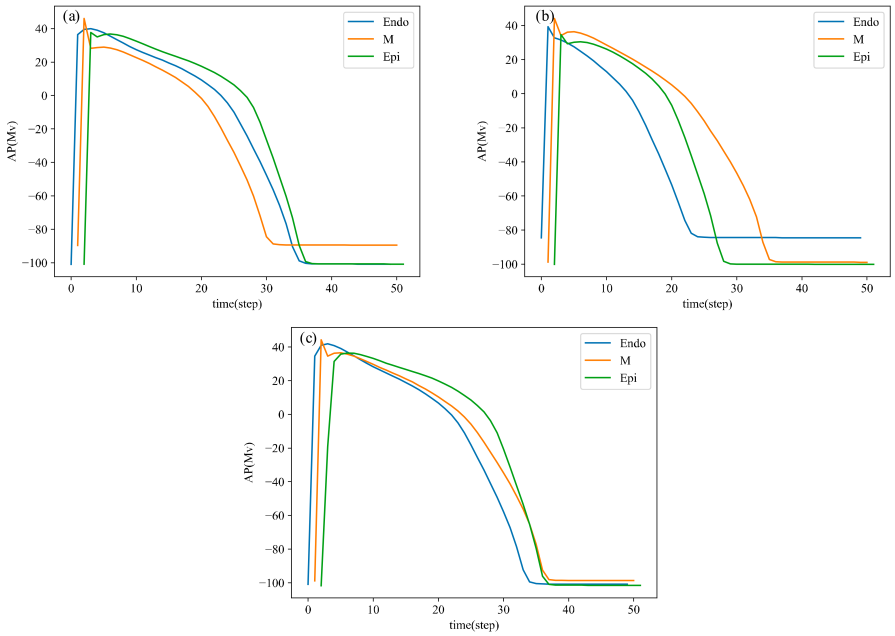

Figure 17. Abnormal ventricular action potentials leading to T-wave inversion. The x-axis represents the time (Step) and the y-axis represents the potential (mV). Moreover, (**a**) is the first anomaly (AS1), (**b**) is the second anomaly (AS2), and (**c**) is the third anomaly (AS3).

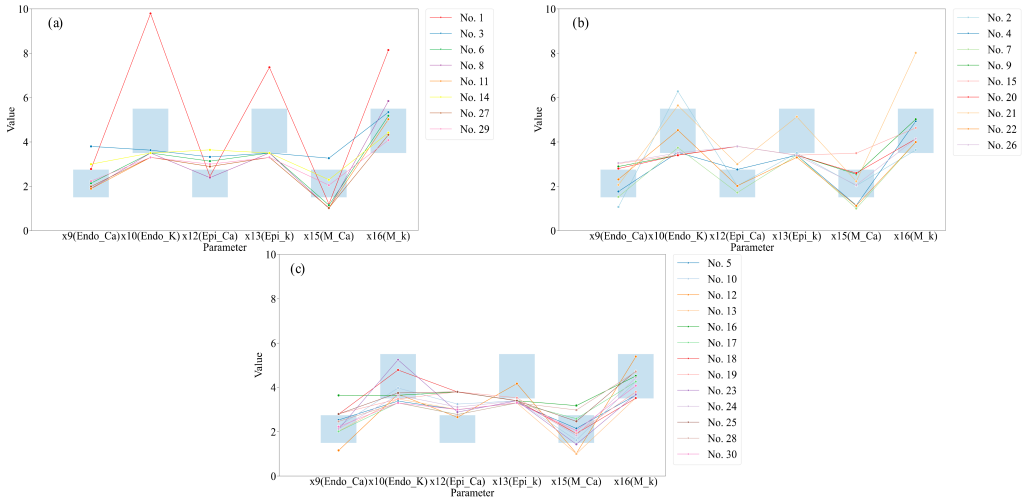

Figure 18. Out of 30 groups of individuals, 8 groups exhibited AS1, as shown in Figures 17a and 18, (**a**). The parameter values of these 8 groups were summarized to obtain 5 possibilities causing this AS1, as shown in Table 6. There are 9 groups exhibiting AS2, as shown in Figures 17b and 18 (**b**). The parameter values of these 9 groups were summarized to obtain the 5 possibilities causing this AS2, as shown in Table 7. Thirteen groups exhibited AS3, as shown in Figures 17c and 18 (**c**). Summarizing the parameter values for these 13 groups yielded 8 possibilities for causing this AS3, as shown in Table 8.

Table 6. The parameter abnormality that may cause AS1.

	x_9	x_{10}	x_{12}	x_{13}	x_{15}	x_{16}
1	▲	▲	○	▲	▼	▲
2	▲	○	▲	▼	▲	○
3	▲	○	▲	▼	○	○
4	○	▼	▲	▼	○	○
5	○	▼	▲	▼	▼	○

▲ indicates above the normal range, ▼ indicates below the normal range, and ○ indicates within the normal range (the same applies to Tables 7 and 8).

Table 7. The parameter abnormality that may cause AS2.

	x_9	x_{10}	x_{12}	x_{13}	x_{15}	x_{16}
1	▼	▲	○	▼	○	○
2	○	○	○	▼	▼	○
3	○	▼	▲	▼	▼	○
4	○	▲	▲	○	○	▲
5	▲	▼	▲	▼	○	○

Table 8. The parameter abnormality that may cause AS3.

	x_9	x_{10}	x_{12}	x_{13}	x_{15}	x_{16}
1	▲	○	▲	▼	▲	○
2	▲	○	▲	▼	○	○
3	▲	▼	▲	○	○	○
4	○	▼	▲	▼	○	○
5	○	▼	▲	▼	▲	○
6	○	○	▲	▼	○	○
7	○	○	▲	▼	▼	○
8	▼	○	○	○	▼	○

In addition, the anomaly parameters of T-wave inversion were statistically analyzed at the 95% confidence level to obtain the confidence intervals, as shown in Tables 9–11.

Table 9. Parameters of confidence intervals for which a 95% confidence level may result in AS1.

	x_9	x_{10}	x_{12}	x_{13}	x_{15}	x_{16}
Confidence Interval	[1.9, 3.1]	[2.4, 6.1]	[2.6, 3.3]	[1.9, 4.7]	[0.9, 2.3]	[4.2, 6]

Table 10. Parameters of confidence intervals for which a 95% confidence level may result in AS2.

	x_9	x_{10}	x_{12}	x_{13}	x_{15}	x_{16}
Confidence Interval	[1.73, 2.81]	[3.32, 4.95]	[2.36, 3.68]	[3.13, 4.07]	[1.45, 2.74]	[3.72, 5.77]

Table 11. Parameters of confidence intervals for which a 95% confidence level may result in AS3.

	x_9	x_{10}	x_{12}	x_{13}	x_{15}	x_{16}
Confidence Interval	[2.01, 2.73]	[3.52, 4.14]	[2.67, 3.91]	[3.11, 3.45]	[1.64, 2.43]	[3.83, 4.54]

4. Discussion

The synergistic study of forward and reverse problems has always been an important direction in the field of biomedical engineering, and in-depth analysis of the formation mechanism of ECG not only helps to reveal the nature of cardiac pathophysiology and physiology, as well as to optimize clinical diagnosis and treatment strategies, but also provides theoretical support for precision medicine. However, the existing methods still face key challenges such as oversimplification of models and difficulty in quantification of parameters in the reverse analysis of electrophysiological parameters in cardiomyocytes from surface ECG signals. In this study, a dual-path research framework integrating forward modeling and inverse optimization was constructed, and the association mechanism between T-wave inversion and abnormal Ca^{2+} and K^{+} plasma concentrations was quantitatively revealed at the cellular scale for the first time.

Figures 7 and 8 provide the results of simulating and verifying the forward generation of a normal ECG. Figure 7 demonstrates the electrical conduction of the cardiac signal.

At 10 ms, the sinus node begins depolarization, which subsequently propagates to the left atrium for depolarization at 40 ms. By 120 ms, depolarization is complete in all atria. Between 220 ms and 230 ms, the subendocardial layer of the ventricular myocardium, M cells, and epicardial cells complete depolarization. The ventricle undergoes repolarization between 420 ms and 520 ms, when a separation of transmembrane potentials occurs in the myocardium $V_M > V_{Endo} > V_{Epi}$. The simulated conduction process is consistent with the normal physiological conduction process [38]. Figure 8 and Table 2 demonstrate the normal ECG waveforms obtained by simulation, with the appropriate parameters set according to the clinical data. In the ECG, the P-wave is generated by the difference in transmembrane potential between atrial and atrial cells; the QRS wave cluster and T-wave are caused by the difference in transmembrane potential between Epi cells, M cells and Endo cells during depolarization and repolarization, respectively. The simulation results meet the diagnostic criteria for normal ECG waveforms [39].

Figures 9 and 10 present the results of simulating and validating the ECG for forward generation of abnormalities. Figure 9 provides validation of the stability of the multiscale model in the presence of multiple electrolyte abnormalities. Figure 9a,b demonstrate the effect of the extracellular Ca^{2+} concentration on the APD, which shortens with an increasing Ca^{2+} concentration, which is in agreement with the medical findings of Severi et al. [35]. Figure 9c,d demonstrate the effect of K^+ channel blockade on the ECG, with prolongation of the QT interval and reduction of the T-wave amplitude of the ECG with deepening of the block. Figure 9e–g demonstrate the effect of Na^+ channel blockade on the ECG, with prolongation of the QT interval and widening of the QRS interval of the ECG with deepening of the block, in agreement with the medical findings of Zemzemi et al. [40]. Afterwards, we adjusted the K^+ and Ca^{2+} concentrations in the cellular environment according to the report of Moon et al. [34] and simulated the abnormal ECG shown in Figure 10. The direction of the T-wave was opposite to the main deflection of the QRS wave group and the morphology of the T-wave was arrow-shaped, which was consistent with the conclusions of the report. The results in Figures 7–10 demonstrate that ECGs adapted to changes in electrolyte concentration can be generated using the framework proposed in this paper. The simulation of T-wave inverted ECG demonstrates that the K^+ concentration and Ca^{2+} concentration in cardiomyocytes have an effect on T-wave shape, which is consistent with the findings in the literature [36,41]. In this paper, we found that the cell–tissue–torso stem multiscale model can fully simulate the forward mapping process from electrophysiological parameters to ECG, and it can be used for the study of the ECG waveform generation mechanism when forward simulation is performed.

Figure 11 shows the validation results using several metaheuristic optimization algorithms. Figure 11 compares the optimization results of the DE, NSGA2 and SSA algorithms for 30 groups of normal ECG signals. The DE algorithm has the fastest convergence speed, smaller objective function values compared to the NSGA2 algorithm, and better global optimization ability with a maximum RMSE of 0.086 in 30 groups of individuals compared to the SSA algorithm. The DE algorithm was chosen to optimize the multiscale cardiac model and the RMSE of the normal ECG signals for all 30 groups of individuals was less than 0.1. Figure 15 shows the optimization of the 30 groups of T-wave inverted ECGs using the DE algorithm and the RMSE of the abnormal ECG signals for all 30 groups of individuals was less than 0.2, which indicates that the inverse solving of the normal signals using the intelligent algorithms resulted in a convergence of the results. Figure 13 demonstrates the comparison between the inverse optimization of 30 groups of normal ECGs and the clinically real ECGs using the framework, and Figure 16 demonstrates the comparison between the inverse optimization of 30 groups of T-wave inverted ECGs and

the clinically real ECGs, and the effectiveness to the inverse problem can be intuitively responded to by the degree of curve fitting in the Figure 13.

Figure 12 shows the results of the inverse solution performed for 30 groups of normal individuals, with outliers in the variable $x_1, x_{13}, x_{16}, x_{18}, x_{19}, x_{24}$, which are specifically analyzed. Among them, x_1 is a dimensionless parameter, where its role is to adjust the size of the ECG, the general clinical situation R wave should be between 0.5 mV and 2.5 mV, the majority of the 30 groups in this 1 mV or less, but in the 28th group of the R wave of 2.1 mV, at this time x_1 there are outliers, but they belong to the normal situation; x_{13}, x_{16} is the extracellular K^+ concentration of the epicardial myocyte and the M cell, respectively, in the 23rd group of ECGs, which found that $x_{13} = 7.1(\text{mmol/L})$ $x_{16} = 7.8(\text{mmol/L})$, the 30th group of ECGs found that, the 3rd group of ECGs of, the ventricular myocyte out of concentration. ECG found $x_{16} = 7.8(\text{mmol/L})$, $x_{13} = 7.3(\text{mmol/L})$ in the group 3 ECG, the extracellular K^+ concentration in ventricular myocytes was too high and was an outlier, but the ventricular repolarization sequence was unchanged and the electrocardiogram was normal in the case of other parameters that were not outliers. x_{18}, x_{19} are the cell length and cell radius of the ventricular myocyte, because everyone has differences in length and radius, and cardiomyocytes have self-regulation. These two outliers are also normal. For the atrial extracellular Na^+ ion concentration, most of the concentration is at 140 (mmol/L); the outlier value is at 135 (mmol/L), but it is also within the normal range. A special case can be seen in which x_{13}, x_{16} shows an abnormal value but a normal ECG, which is possible in clinical situations. This situation cannot be diagnosed by ECG and needs further examination to confirm. The solved data of 30 groups of normal individuals were counted to obtain specific ranges of 29 physiological parameters at the cellular level in Table 4, which are basically within the clinical reference range of [37,42] and are used as a measure of normal ECG activity.

The results of the inverse solution for 30 groups of T-wave inverted individuals are given in Figures 17 and 18. The inverse solution revealed abnormalities in the K^+ concentration and Ca^{2+} concentration of the ventricular myocytes, which were manifested by the fact that the order of action potential repolarization in the ventricular myocardium differed from that of the normal condition in Figure 8a, which was consistent with previous studies showing that the mechanism of T-wave inversion formation was caused by abnormalities of the potential difference generated by the ventricular repolarization, and that this abnormality is in turn caused by abnormal extracellular ion concentrations in ventricular myocytes [43]. In this paper, the abnormalities were classified into three cases based on the difference in negative potentials: AS1 for $V_{Epi} > V_{Endo} > V_M$; AS2 for $V_M > V_{Epi} > V_{Endo}$; and AS3 for $V_{Epi} > V_M > V_{Endo}$. Figure 18 demonstrates the distribution of the ventricular Endo cell, Epi cell, and M cell K^+ concentrations and Ca^{2+} concentrations for the three conditions. The deviations of abnormal parameters from the normal range are counted in Tables 6–8 and quantified in Tables 9–11 at the 95% confidence intervals. In the AS1 abnormality, there was a significant difference between x_{10}, x_{12} and x_{13} and the range of normal values. In the AS2 abnormality, x_{12} and x_{13} were significantly different from the normal value range. In the AS3 abnormality, x_9, x_{12} and x_{13} were significantly different from the normal value range. Therefore, it is considered 95% likely that the inversion of the T-wave is caused by abnormalities in these parameters. These abnormalities are caused by a change in the balance of the K^+ and Ca^{2+} concentrations and are ultimately reflected in the ventricular action potentials and ECG.

Table 5 presents a comparison with existing ECG inverse methods. In this study, a differential evolutionary algorithm was used to optimize the parameters of the multiscale model to achieve the ECG inverse solution on a cellular scale. In contrast to the numerical approach of Barnes et al. [16], the electrophysiological properties of ion channel exchange

in the heart are considered in this study. In contrast to the methods proposed by Sahli Costabal [17] and Tenderini [18], this method allows us to explain the pathological mechanisms of the different structures of the ventricle on a cellular scale. Additionally, the algorithmic framework proposed in this paper has structural advantages in that the choice of atrial and ventricular models, as well as the solution of the optimization algorithm, can be made flexibly to allow for research and subsequent model improvement for different cardiovascular diseases.

We found that the mechanism of T-wave inversion is related to the concentration of K^+ and Ca^{2+} in the extracellular fluid of ventricular myocytes. This approach could provide decision support for clinicians, enhance early detection and prediction of heart disease, and provide personalized diagnosis and treatment for different patients.

5. Conclusions

In this study, we proposed a novel methodological framework that successfully integrates a multiscale cardiac electrophysiological forward model (cell–tissue–torso) with an inverse optimization technique using the DE algorithm. The forward model accurately reproduced the propagation of action potentials and generated realistic body surface ECGs. Furthermore, the inverse solution effectively minimized the RMSE to quantify cellular-scale parameters from macroscopic ECG data. By applying this framework to clinical data, we specifically quantified the ionic mechanisms underlying T-wave inversion. Compared with normal electrocardiographic parameters, different degrees of abnormal K^+ and Ca^{2+} concentrations in the extracellular fluid of the ventricular myocardium were observed in the T-wave inversion, which led to three different abnormalities during ventricular repolarization: (1) $V_{Epi} > V_{Endo} > V_M$, higher Ca^{2+} concentrations and K^+ concentration is lower (95% confidence interval $[Ca^{2+}]$: 2.60 to 3.30 (mmol/L), $[K^+]$: 1.9 to 4.7 (mmol/L)); (2) $V_M > V_{Epi} > V_{Endo}$, with a higher Ca^{2+} concentration and a lower K^+ concentration (95% confidence interval $[Ca^{2+}]$: 2.36 to 3.68 (mmol/L), $[K^+]$: 3.13 to 4.07 (mmol/L)); and (3) $V_{Epi} > V_M > V_{Endo}$, higher concentrations of Ca^{2+} and lower concentrations of $[K^+]$ (95% confidence interval $[Ca^{2+}]$: 2.67 to 3.91(mmol/L), $[K^+]$: 3.11 to 3.45 (mmol/L)).

The results of this study provide valuable insights into understanding the mechanisms of T-wave inversion in the electrocardiogram, thereby deepening the understanding of the relationship between T-wave inversion and the electrical activity of the heart. In addition, these findings open up new avenues for the development of drugs for the treatment of T-wave inversion. Meanwhile, the methodology used in this study can also be used to study the mechanisms of other abnormal ECGs, which can help physicians to make early diagnosis and interventions for diseases.

Author Contributions: Conceptualization, T.G.; methodology, T.G.; validation, T.G., J.Z. and Y.L.; formal analysis, T.G. and Y.L.; investigation, T.G. and J.Z.; resources, T.G.; data curation, T.G.; writing—original draft preparation, T.G.; writing—review and editing, J.Z.; visualization, T.G. and Y.L.; supervision, J.Z.; project administration, J.Z.; funding acquisition, T.G. All authors have read and agreed to the published version of the manuscript.

Funding: This research received no external funding.

Data Availability Statement: The data presented in this study are available on request from the corresponding author. The data are not publicly available due to patient privacy and ethical restrictions associated with clinical medical records.

Conflicts of Interest: The authors declare no conflicts of interest.

References

1. Yang, X.L.; Liu, G.Z.; Tong, Y.H.; Yan, H.; Xu, Z.; Chen, Q.; Liu, X.; Zhang, H.-H.; Wang, H.-B.; Tan, S.-H. The history, hotspots, and trends of electrocardiogram. *J. Geriatr. Cardiol.* **2015**, *12*, 448. [CrossRef]
2. Costa, R.; Winkert, T.; Manhães, A.; Teixeira, J.P. QRS peaks, P and T waves identification in ECG. *Procedia Comput. Sci.* **2021**, *181*, 957–964. [CrossRef]
3. D'Ascenzi, F.; Anselmi, F.; Berti, B.; Capitani, E.; Chiti, C.; Franchini, A.; Graziano, F.; Nistri, S.; Focardi, M.; Capitani, M.; et al. Prevalence and significance of T-wave inversion in children practicing sport: A prospective, 4-year follow-up study. *Int. J. Cardiol.* **2019**, *279*, 100–104. [CrossRef]
4. Azab, D.; Zahran, M.E.; Elmahmoudy, A. Initial T wave morphology in the chest leads in patients presenting with anterior ST-segment elevation myocardial infarction and its correlation with spontaneous reperfusion of the left anterior descending coronary artery. *Int. J. Cardiovasc. Acad.* **2019**, *5*, 52–57. [CrossRef] [PubMed]
5. Romero, J.; Alviz, I.; Parides, M.; Diaz, J.C.; Briceno, D.; Gabr, M.; Gamero, M.; Patel, K.; Braunstein, E.D.; Purkayastha, S.; et al. T-wave inversion as a manifestation of COVID-19 infection: A case series. *J. Interv. Card. Electrophysiol.* **2020**, *59*, 485–493. [CrossRef]
6. Williams, D.R.; Cole, S.J. Ventricular fibrillation following butane gas inhalation. *Resuscitation* **1998**, *37*, 43–45. [CrossRef]
7. Said, S.A.M.; Somer, S.T.; Oude Luttikhuis, H.A. Flecainide-induced JT prolongation, T wave inversion and ventricular tachycardia during treatment for symptomatic atrial fibrillation. *Int. J. Cardiol.* **1994**, *44*, 285–287. [CrossRef]
8. Gulrajani, R.M. The forward problem of electrocardiography: From heart models to body surface potentials. In Proceedings of the 19th Annual International Conference of the IEEE Engineering in Medicine and Biology Society, Chicago, IL, USA, 30 October–2 November 1997; pp. 2604–2609. [CrossRef]
9. Antzelevitch, C.; Fish, J. Electrical heterogeneity within the ventricular wall. *Basic Res. Cardiol.* **2001**, *96*, 517–527. [CrossRef] [PubMed]
10. Sicouri, S.; Antzelevitch, C. A subpopulation of cells with unique electrophysiological properties in the deep subepicardium of the canine ventricle: The M cell. *Circ. Res.* **1991**, *68*, 1729–1741. [CrossRef]
11. Sicouri, S.; Fish, J.; Antzelevitch, C. Distribution of M cells in the canine ventricle. *J. Cardiovasc. Electrophysiol.* **1994**, *5*, 824–837. [CrossRef]
12. Ten Tusscher, K.H.W.J.; Bernus, O.; Panfilov, A.V. Comparison of electrophysiological models for human ventricular cells and tissues. *Prog. Biophys. Mol. Biol.* **2006**, *90*, 326–345. [CrossRef]
13. O'Hara, T.; Virág, L.; Varró, A.; Rudy, Y. Simulation of the undiseased human cardiac ventricular action potential: Model formulation and experimental validation. *PLoS Comput. Biol.* **2011**, *7*, e1002061. [CrossRef] [PubMed]
14. Pascual-Sánchez, L.; Goya-Esteban, R.; Cruz-Roldán, F.; Hernández-Madrid, A.; Blanco-Velasco, M. Machine learning based detection of T-wave alternans in real ambulatory conditions. *Comput. Methods Programs Biomed.* **2024**, *249*, 108157. [CrossRef] [PubMed]
15. Rudy, Y.; Oster, H.S. The electrocardiographic inverse problem. *Crit. Rev. Biomed. Eng.* **1992**, *20*, 25–45.
16. Barnes, J.P.; Johnston, P.R. Application of robust generalised cross-validation to the inverse problem of electrocardiology. *Comput. Biol. Med.* **2016**, *69*, 213–225. [CrossRef]
17. Sahli Costabal, F.; Yang, Y.; Perdikaris, P.; Hurtado, D.E.; Kuhl, E. Physics-informed neural networks for cardiac activation mapping. *Front. Phys.* **2020**, *8*, 42. [CrossRef]
18. Tenderini, R.; Pagani, S.; Quarteroni, A.; Deparis, S. PDE-aware deep learning for inverse problems in cardiac electrophysiology. *SIAM J. Sci. Comput.* **2022**, *44*, B605–B639. [CrossRef]
19. Neha, F.; Bhati, D.; Shukla, D.K.; Amiruzzaman, M. From classical techniques to convolution-based models: A review of object detection algorithms. In Proceedings of the IEEE 6th International Conference on Image Processing, Applications and Systems (IPAS), Lyon, France, 9–11 January 2025; pp. 1–6. [CrossRef]
20. Grandi, E.; Pandit, S.V.; Voigt, N.; Workman, A.J.; Dobrev, D.; Jalife, J.; Bers, D.M. Human atrial action potential and Ca^{2+} model: Sinus rhythm and chronic atrial fibrillation. *Circ. Res.* **2011**, *109*, 1055–1066. [CrossRef]
21. Luo, C.; Rudy, Y. A model of the ventricular cardiac action potential: Depolarization, repolarization, and their interaction. *Circ. Res.* **1991**, *68*, 1501–1526. [CrossRef]
22. Bartolucci, C.; Passini, E.; Hyttinen, J.; Paci, M.; Severi, S. Simulation of the effects of extracellular calcium changes leads to a novel computational model of human ventricular action potential with a revised calcium handling. *Front. Physiol.* **2020**, *11*, 314. [CrossRef]
23. Hodgkin, A.L.; Huxley, A.F. A quantitative description of membrane current and its application to conduction and excitation in nerve. *J. Physiol.* **1952**, *117*, 500. [CrossRef]
24. Greenberg, J.M.; Hastings, S.P. Spatial patterns for discrete models of diffusion in excitable media. *SIAM J. Appl. Math.* **1978**, *34*, 515–523. [CrossRef]

25. Que, W.; Han, C.; Zhao, X.; Shi, L. An ECG generative model of myocardial infarction. *Comput. Methods Programs Biomed.* **2022**, *225*, 107062. [CrossRef] [PubMed]
26. Luo, C.-J.; You, T.-T.; Liu, T.; Ying, H.; Wang, K.-Q.; Zhang, H.-G. Virtual electrophysiological heart model and atrial fibrillation: A review. *Prog. Biochem. Biophys.* **2019**, *46*, 976–992. [CrossRef]
27. Zhu, H.; Sun, Y.; Rajagopal, G.; Mondry, A.; Dhar, P. Facilitating arrhythmia simulation: The method of quantitative cellular automata modeling and parallel running. *Biomed. Eng. Online* **2004**, *3*, 29. [CrossRef] [PubMed]
28. Martínez-Arranz, I.; Alonso, C.; Mayo, R.; Mincholé, I.; Mato, J.M.; Lee, D.-J. Genetic algorithms applied to translational strategy in metabolic-dysfunction associated steatohepatitis (MASH): Learning from mouse models. *Comput. Methods Programs Biomed.* **2024**, *255*, 108346. [CrossRef] [PubMed]
29. Storn, R.; Price, K. Differential evolution—A simple and efficient heuristic for global optimization over continuous spaces. *J. Glob. Optim.* **1997**, *11*, 341–359. [CrossRef]
30. Xue, J.; Shen, B. A novel swarm intelligence optimization approach: Sparrow search algorithm. *Syst. Sci. Control Eng.* **2020**, *8*, 22–34. [CrossRef]
31. Ao, Y.; Chi, H. Experimental study on differential evolution strategies. In Proceedings of the 2009 WRI Global Congress on Intelligent Systems, Xiamen, China, 19–21 May 2009; pp. 19–24. [CrossRef]
32. Yang, X.; Liu, J.; Liu, Y.; Xu, P.; Yu, L.; Zhu, L.; Chen, H.; Deng, W. A novel adaptive sparrow search algorithm based on chaotic mapping and t-distribution mutation. *Appl. Sci.* **2021**, *11*, 11192. [CrossRef]
33. Harris, P.R.E. The normal electrocardiogram: Resting 12-lead and electrocardiogram monitoring in the hospital. *Crit. Care Nurs. Clin.* **2016**, *28*, 281–296. [CrossRef]
34. Moon, H.S.; Lee, S.K.; Chung, J.H.; In, C.B. Hypocalcemia and hypokalemia due to hyperventilation syndrome in spinal anesthesia: A case report. *Korean J. Anesthesiol.* **2011**, *61*, 519–523. [CrossRef]
35. Severi, S.; Corsi, C.; Cerbai, E. From in vivo plasma composition to in vitro cardiac electrophysiology and in silico virtual heart: The extracellular calcium enigma. *Philos. Trans. R. Soc. A* **2009**, *367*, 2203–2223. [CrossRef] [PubMed]
36. Poelzing, S.; Veeraraghavan, R. Heterogeneous ventricular chamber response to hypokalemia and inward rectifier potassium channel blockade underlies bifurcated T wave in guinea pig. *Am. J. Physiol. Heart Circ. Physiol.* **2007**, *292*, H3043–H3051. [CrossRef] [PubMed]
37. Konstam, M.A. Hyperkalaemia in heart failure: Binding the patient to improved treatment? *Eur. J. Heart Fail.* **2015**, *17*, 997–999. [CrossRef]
38. van Weerd, J.H.; Christoffels, V.M. The formation and function of the cardiac conduction system. *Development* **2016**, *143*, 197–210. [CrossRef]
39. Ware, W.A.; Bonagura, J.D.; Scansen, B.A. Electrocardiography. In *Cardiovascular Disease in Companion Animals*; CRC Press: Boca Raton, FL, USA, 2021; pp. 135–166. [CrossRef]
40. Zemzemi, N.; Bernabeu, M.O.; Saiz, J.; Cooper, J.; Pathmanathan, P.; Mirams, G.R.; Pitt-Francis, J.; Rodriguez, B. Computational assessment of drug-induced effects on the electrocardiogram: From ion channel to body surface potentials. *Br. J. Pharmacol.* **2013**, *168*, 718–733. [CrossRef]
41. Ahmed, R.; Yano, K.; Mitsuoka, T.; Ikeda, S.; Ichimaru, M.; Hashiba, K. Changes in T wave morphology during hypercalcemia and its relation to the severity of hypercalcemia. *J. Electrocardiol.* **1989**, *22*, 125–132. [CrossRef]
42. Urso, C.; Brucculeri, S.; Caimi, G. Acid–base and electrolyte abnormalities in heart failure: Pathophysiology and implications. *Heart Fail. Rev.* **2015**, *20*, 493–503. [CrossRef]
43. Yan, G.X.; Antzelevitch, C. Cellular basis for the normal T wave and the electrocardiographic manifestations of the long-QT syndrome. *Circulation* **1998**, *98*, 1928–1936. [CrossRef] [PubMed]